High Efficiency Pb–In Binary Metal Perovskite Solar Cells

Zhao-Kui Wang, Meng Li, Ying-Guo Yang, Yun Hu, Heng Ma, Xing-Yu Gao, and Liang-Sheng Liao**

Since the invention of crystalline silicon solar cells in the 1950s,[1] many new types of light harvesting materials, including amorphous and polycrystalline semiconductors, organic and metal complex dyes, and organic semiconductors, have been developed.[2,3] However, several issues such as high production and installation costs and/or unsatisfactory efficiency decrease their economic feasibility and hamper their widespread use.[4,5] The rise of organometal halide perovskite solar cells brings a very competitive and fascinating prospect on photovoltaic commercialization via their unimaginable efficiency racing.[6–14] Presently, certified power conversion efficiency (PCE) approached above 20%[12] since the initial report of 3.8% in 2009.[6]

Noticeably, lead halides have to be utilized in most state-of-the-art perovskite-based devices. The presence of lead could create toxicological issues to the environment in the future. New materials that can replace or substitute the lead without sacrificing the device performance are thus desirable. Sn, Ge, and members of the group IVA elements are regarded as the most viable replacements for Pb in perovskite materials. Particularly, Sn is assumed to be a potential choice of Pb-free perovskite solar cells because both Sn and Pb belong to the IVA group and have similar physical and chemical characteristics. Recently, Sn and/or Sn–Pb binary metal-based organometal halide perovskites have been reported theoretically and experimentally.[15–23] Despite great efforts, pure Sn-based perovskite solar cells demonstrate limited PCE around 7% because of the poor film crystallization and film coverage, which is assumed to be derived from the inherent instability of the Sn^{2+} ion in the presence of oxygen and moisture.[15–18] Sn–Pb binary metal perovskites demonstrate extended band gap by varying the Sn-to-Pb ratio. However, these binary metal-based perovskite solar cells exhibit nonstriking PCE less than 10% up to date.[20–22] As a matter of fact, no satisfactory replacements and/or substitutes for Pb in organometal halide perovskites have yet been reported. Further efforts to seek other replacements or substitutes for achieving lead-free and/or less-lead perovskite solar cells with high PCE and stability are necessary.

Indium (In) is a post-transition metallic element which locates diagonally adjacent to Pb. Most commonly, indium loses its three outermost electrons and becomes indium(III) ions (In^{3+}) with a stable oxidation state. Indium(III) chloride ($InCl_3$) is a representative indium halide with good solubility. Herein, moving from the idea of replacing Pb atoms with other alternative metals, we propose and investigate an alternative mixed organic–inorganic perovskite, $CH_3NH_3Pb_{1-a}In_aI_3Cl_a$, where parts of Pb(II) atoms are substituted by In(III). A substantially improved PCE of 17.55% in a planar heterojunction device based on this system has been achieved compared with 12.61% in a pure-lead-based control device. Pb–In perovskites exhibit a good crystal quality with multiple ordered crystal orientations, which has been revealed by grazing incidence X-ray diffraction (GIXRD) technique. Consequently, the improved crystal quality gives rise to enhanced short-circuit current density (21.90 vs 19.07 mA cm^{-2}), open-circuit voltage (1.03 vs 0.91 V), and fill factor (FF, 0.78 vs 072). We believe this is the first report on Pb–In binary metal perovskite solar cells with PCE exceeding 17.5%.

X-ray diffraction (XRD) patterns of pure Pb $CH_3NH_3PbI_xCl_{3-x}$ and binary Pb–In perovskite $CH_3NH_3Pb_{1-a}In_aI_3Cl_a$ are shown in Figure S1 (Supporting Information), where a is 0, 0.05, 0.1, 0.15, 0.2, and 0.25. Even heavy substituted, Pb–In perovskite samples present similar diffraction peaks as the pure Pb-based one. Enlarged XRD patterns of 22°–27° are shown in Figure S2 (Supporting Information). There are two peaks, 23.4° and 24.4°, which could be indexed to (211) and (202) planes in the tetragonal *I4 cm* space group, in this range for all samples. It agrees well with the reported $MAPbI_3$ structure at room temperature.[20,24,25] Unlike Pb–Sn perovskites, no obvious phase transition was observed in Pb–In perovskites with varied substituting ratio. Perovskite solar cells adopt a planar heterojunction structure as shown in **Figure 1**. Poly(3,4-ethylenedioxy-thiophene)-poly(styrene sulfonate) (PEDOT:PSS) and phenyl-C61-butyric acid methyl ester ($PC_{61}BM$) are used as hole and electron transport layers, respectively.[26] Bathophenanthroline (Bphen) is used as a cathode interfacial layer for cathode interface modification.[27] Perovskite precursor solution is prepared by dissolving CH_3NH_3I, $PbCl_2$, and $InCl_3$ in *N,N*-dimethylformamide (DMF) with a molar ratio of 3:(1–a):a. The precursor solution is spin-coated onto PEDOT:PSS. Crystal

Dr. Z.-K. Wang, M. Li, Y. Hu, Prof. L.-S. Liao
Jiangsu Key Laboratory for Carbon-Based Functional Materials and Devices
Institute of Functional Nano and Soft Materials (FUNSOM)
Soochow University
Suzhou, Jiangsu 215123, P. R. China
E-mail: lsliao@suda.edu.cn
Dr. Y.-G. Yang, Prof. X.-Y. Gao
Shanghai Synchrotron Radiation Facility
Shanghai Institute of Applied Physics
Chinese Academy of Sciences
Shanghai 201204, P. R. China
E-mail: gaoxingyu@sinap.ac.cn
Prof. H. Ma
College of Physics and Electronic Engineering
Henan Normal University
Xinxiang, Henan 453007, P. R. China

DOI: 10.1002/adma.201600626

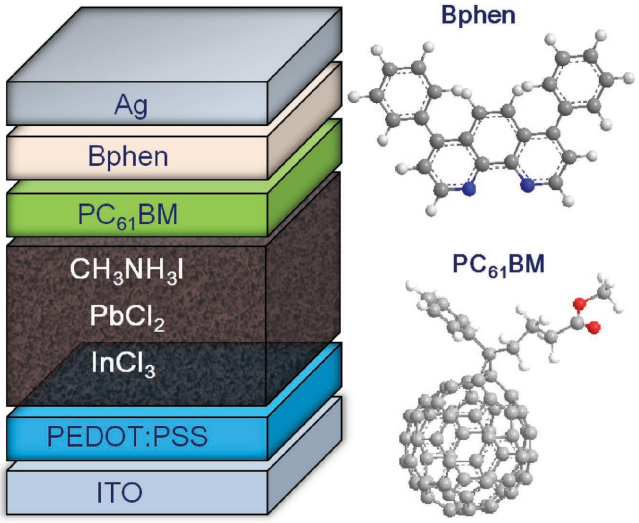

Figure 1. Device configuration of planar heterojunction perovskite solar cells, and the molecule structures of the interfacial materials of $PC_{61}BM$ and Bphen.

perovskite films were obtained by annealing with a typical gradient increased temperature method.[25–27] $PC_{61}BM$ and Bphen were spin-coated sequentially without additional annealing. The Ag electrode was finally deposited onto the Bphen layer through a shadow mask. Except PEDOT:PSS and Ag layers, the spin-coating of all other layers was carried out in a nitrogen glovebox to avoid hydrolysis and oxidation.

The $InCl_3$ substituting ratio has a strong impact on the device performance of $CH_3NH_3Pb_{1-a}In_aI_3Cl_a$ perovskite solar cells (Figure S3, Supporting Information). **Table 1** summarizes the cell parameters including short-circuit current density (J_{SC}), open-circuit voltage (V_{OC}), FF, and PCE. As examples, **Figure 2**a plots the current density–voltage (J–V) characteristics of $CH_3NH_3Pb_{0.85}In_{0.15}I_3Cl_{0.15}$ and controlled $CH_3NH_3PbI_xCl_{3-x}$ perovskite solar cells under AM 1.5 G illumination with a light intensity of 100 mW cm^{-2}. Three key parameters J_{SC}, V_{OC}, and FF increase simultaneously with indium substituting ratio. Under an optimized case of $Pb_{0.85}In_{0.15}$, the device presents a maximum PCE of 17.55% with a J_{SC} of 21.90 mA cm^{-2}, a V_{OC} of 1.03 V, and an FF of 0.78. Relevant results for the $CH_3NH_3PbI_xCl_{3-x}$ perovskite solar cell are PCE = 12.61%, J_{SC} = 19.07 mA cm^{-2}, V_{OC} = 0.91 V, and FF = 0.72. Over 25 $CH_3NH_3Pb_{0.85}In_{0.15}I_3Cl_{0.15}$ based devices were fabricated and tested for verifying the reproducibility of high efficiency. As shown by the histograms (the inset of Figure 2a), PCE followed a Gaussian distribution with small relative standard deviations. Unfortunately, when completely replacing $PbCl_2$ by $InCl_3$, the device shows very poor performance with a PCE only of 0.013%. We ascribe it to the very weak absorption (Figure S4, Supporting Information) and the inferior crystallinity (Figure S1, Supporting Information) in CH_3NH_3I:$InCl_3$ (3:1) based films. Figure 2b presents the UV–vis absorption spectra of the stacked films of $CH_3NH_3PbI_xCl_{3-x}$ and $CH_3NH_3Pb_{0.85}In_{0.15}I_3Cl_{0.15}$ films on PEDOT:PSS. Light absorption enhancement was observed in almost the whole visible spectral range. Actually, absorption of $CH_3NH_3Pb_{0.85}In_{0.15}I_3Cl_{0.15}$ films enhances with indium substituting ratio (Figure S4, Supporting Information). Higher external quantum efficiency spectrum of $CH_3NH_3Pb_{0.85}In_{0.15}I_3Cl_{0.15}$ based device is observed compared with that of the $CH_3NH_3PbI_xCl_{3-x}$ based one (Figure 2c). In addition, $CH_3NH_3Pb_{0.85}In_{0.15}I_3Cl_{0.15}$ based device demonstrated more stable PCE performance than that of the control device (Figure 2d). After 350 h of air exposure, $CH_3NH_3Pb_{0.85}In_{0.15}I_3Cl_{0.15}$ based device reached the half-efficiency (half of initial efficiency of the fresh devices), whereas the PCE of the control device yet degraded to one-tenth of the initial value. The improved stability is attributed to more stable In^{3+} oxidation states in $CH_3NH_3Pb_{0.85}In_{0.15}I_3Cl_{0.15}$ perovskites. Perovskite solar cells with TiO_2-based normal structure were also fabricated to demonstrate the applicability of our method. The results indicate that our method of introducing $InCl_3$ into perovskites is feasible for improving the device performance in both inverted- and normal-structure perovskite solar cells (Figure S5 and Table S1 of the Supporting Information).

Remarkable increase of PCE from 12.61% to 17.55% is achieved by 15% (molar ratio) $InCl_3$ replacement of $PbCl_2$. The nature behind the large boost in cell performance could be worthwhile to study. Actually, film morphology including uniformity and coverage, and crystal quality in terms of grain size and crystal orientation are regarded as the two key factors in achieving high-performance perovskite solar cells.[28–37] Therefore, both morphology and crystallinity of the perovskite film were investigated by scanning electron microscopy (SEM), XRD, and GIXRD techniques. **Figure 3**a,b shows the SEM images of $CH_3NH_3PbI_xCl_{3-x}$ and $CH_3NH_3Pb_{0.85}In_{0.15}I_3Cl_{0.15}$ films, respectively. The morphological difference between the two samples is very evident. The perovskite films made from pure $PbCl_2$ route demonstrate good quality with features of laminar structure and large grain sizes (2–5 μm). However, there exist many pinholes in the film, which would be adverse

Table 1. Perovskite solar cell performance parameters.

Perovskites	J_{SC} [mA cm^{-2}]	$J_{SC\text{-}AVE}$ [mA cm^{-2}]	V_{OC} [V]	FF	PCE [%]	PCE_{AVE} [%]
$MAPbI_xCl_{3-x}$	19.07	19.12 ± 0.22	0.91	0.72	12.61	12.29 ± 0.36
$MAPb_{0.95}In_{0.05}I_3Cl_{0.05}$	20.95	20.96 ± 0.08	0.93	0.73	14.22	14.05 ± 0.15
$MAPb_{0.90}In_{0.10}I_3Cl_{0.10}$	21.61	21.71 ± 0.11	0.96	0.77	15.94	15.66 ± 0.26
$MAPb_{0.85}In_{0.15}I_3Cl_{0.15}$	21.90	22.08 ± 0.11	1.03	0.78	17.55	17.34 ± 0.18
$MAPb_{0.80}In_{0.20}I_3Cl_{0.20}$	20.22	20.78 ± 0.98	1.04	0.68	14.31	14.50 ± 0.20
$MAPb_{0.75}In_{0.25}I_3Cl_{0.25}$	15.93	15.31 ± 1.23	1.00	0.65	10.34	9.75 ± 1.13
MAI: $InCl_3$ (3:1)	0.79	0.72 ± 0.11	0.058	0.30	0.013	0.011 ± 0.004

Adv. Mater. **2016**,
DOI: 10.1002/adma.201600626

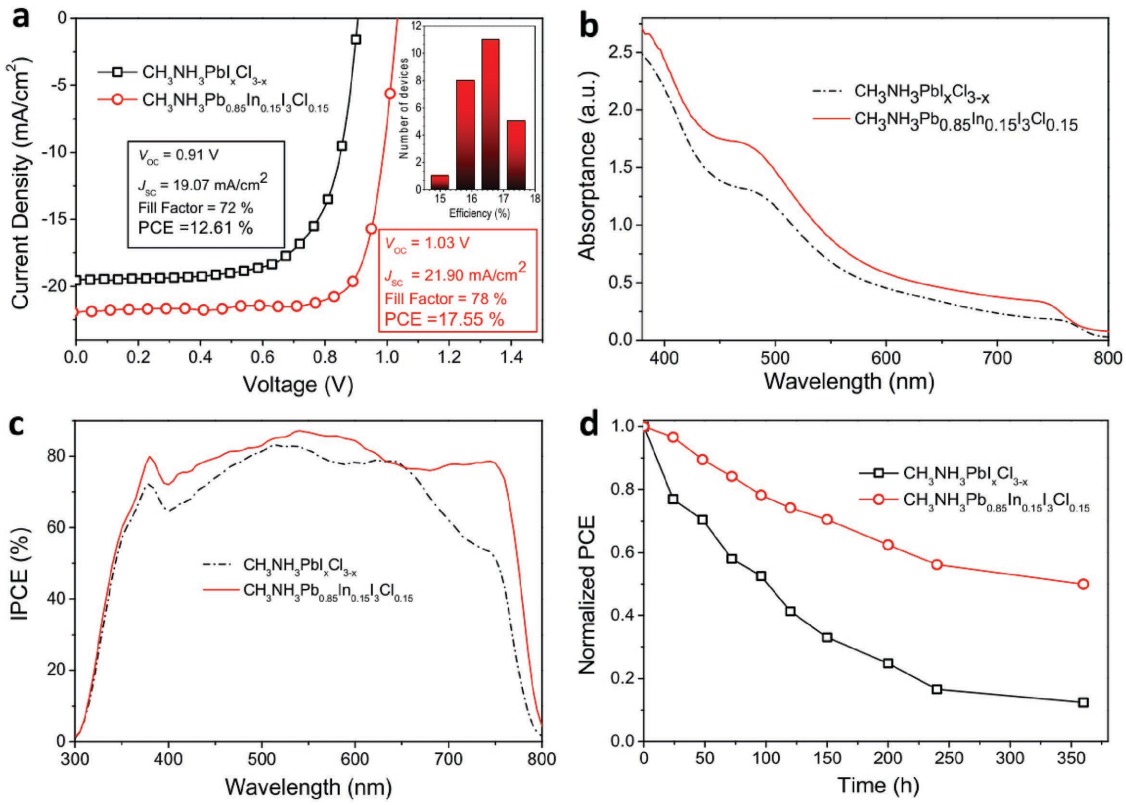

Figure 2. a) *J–V* curves of the best-performing device using $CH_3NH_3Pb_{0.85}In_{0.15}I_3Cl_{0.15}$ and $CH_3NH_3PbI_xCl_{3-x}$ perovskite as the light harvesting layer measured under simulated AM 1.5 sunlight of 100 mW cm^{-2} irradiance. Inset is the histogram of PCEs in $CH_3NH_3Pb_{0.85}In_{0.15}I_3Cl_{0.15}$ based devices measured over 25 cells. b) UV–vis absorbance spectra of $CH_3NH_3Pb_{0.85}In_{0.15}I_3Cl_{0.15}$ and $CH_3NH_3PbI_xCl_{3-x}$ perovskites onto ITO/PEDOT:PSS underlayers. c) Incident photon-to-electron conversion efficiency (IPCE) of $CH_3NH_3Pb_{0.85}In_{0.15}I_3Cl_{0.15}$ and $CH_3NH_3PbI_xCl_{3-x}$ based perovskite solar cells. d) Normalized PCE values as a function of exposing time to air.

to the performance of the perovskites. For the route of mixed $PbCl_2$ (85%) and $InCl_3$ (15%), the pore sizes are much smaller and are in the scale of hundreds of nanometers with fewer pinholes. Similar to the cases of perovskites on PEDOT:PSS, Pb–In perovskites onto TiO_2 (compact) films also showed small grain size with fewer pinholes (Figure S6, Supporting Information).

However, we found that the morphology change or pinholes' reduction is not the only factor to the enhancement of the PCE in the devices. As shown in Figure S7 and Table S2 of the Supporting Information, when the $InCl_3$ ratio is increased from 0 to 0.05, the total pinholes' area is reduced by 20% (i.e., the film coverage is increased from 94% to 95.2%) and the PCE is increased by 13% from 12.61% to 14.22%. However, when the $InCl_3$ ratio is increased from 0.05 to 0.15, the total pinholes' area is almost unchanged (i.e., the film coverage is only varied from 95.2% to 95.4%). But the PCE is increased by 16.6% from 14.22% to 17.55%. Therefore, crystal characteristics such as the crystalline orientation of the Pb–In perovskites should be investigated to fully understand the enhancement of the device performance.

In Figure 3c,d, we show the XRD patterns of $CH_3NH_3PbI_xCl_{3-x}$ and $CH_3NH_3Pb_{0.85}In_{0.15}I_3Cl_{0.15}$ perovskite films, respectively. Evidently, the perovskite films fabricated from pure $PbCl_2$ route, and mixed $PbCl_2$ (85%) and $InCl_3$ (15%) route exhibit almost the same diffraction peaks (related to crystallographic planes including (110), (200), (211), (202), (220), (310), (312), (224), and (314)) with respect to the same crystal structure (also reflected in Figure S1 of the Supporting Information). Noticeably, large difference in main peak intensity between the two samples is still recognizable. (110) and (220) are the main peaks in $CH_3NH_3I_xPbCl_{3-x}$ film. It means that $CH_3NH_3PbI_xCl_{3-x}$ film grew preferentially along ⟨110⟩ orientation. However, more than five main peaks including (110), (220), (224), (312), and (310) exist in $CH_3NH_3Pb_{0.85}In_{0.15}I_3Cl_{0.15}$ perovskite film with relatively high intensity. In fact, it is evident to a trend that the peaks locate at (220), (224), (312), and (310) gradually dominate the XRD pattern when increasing the $InCl_3$ ratio (Figure S1, Supporting Information). It therefore suggests that Pb–In binary metal based perovskites grew with multiple and ordered crystal orientations.

However, 1D XRD can provide only limited structural information of the perovskites with different orientations. Further evidence for the multiple ordered crystal orientations of the Pb–In perovskites was obtained from the 2D GIXRD measurements. The real-time diffraction data based on a fast 2D area detector combined with a high brightness synchrotron X-ray source can provide much rich 2D information on the crystal texture and coarsening. **Figure 4**a–d shows the 2D GIXRD profiles of representative perovskite films of $CH_3NH_3PbI_xCl_{3-x}$, $CH_3NH_3Pb_{0.95}In_{0.05}I_3Cl_{0.05}$, $CH_3NH_3Pb_{0.85}In_{0.15}I_3Cl_{0.15}$, and $CH_3NH_3Pb_{0.75}In_{0.25}I_3Cl_{0.25}$. All of the GIXRD patterns exhibited strong scattering backgrounds. In the cases of low $InCl_3$ molar

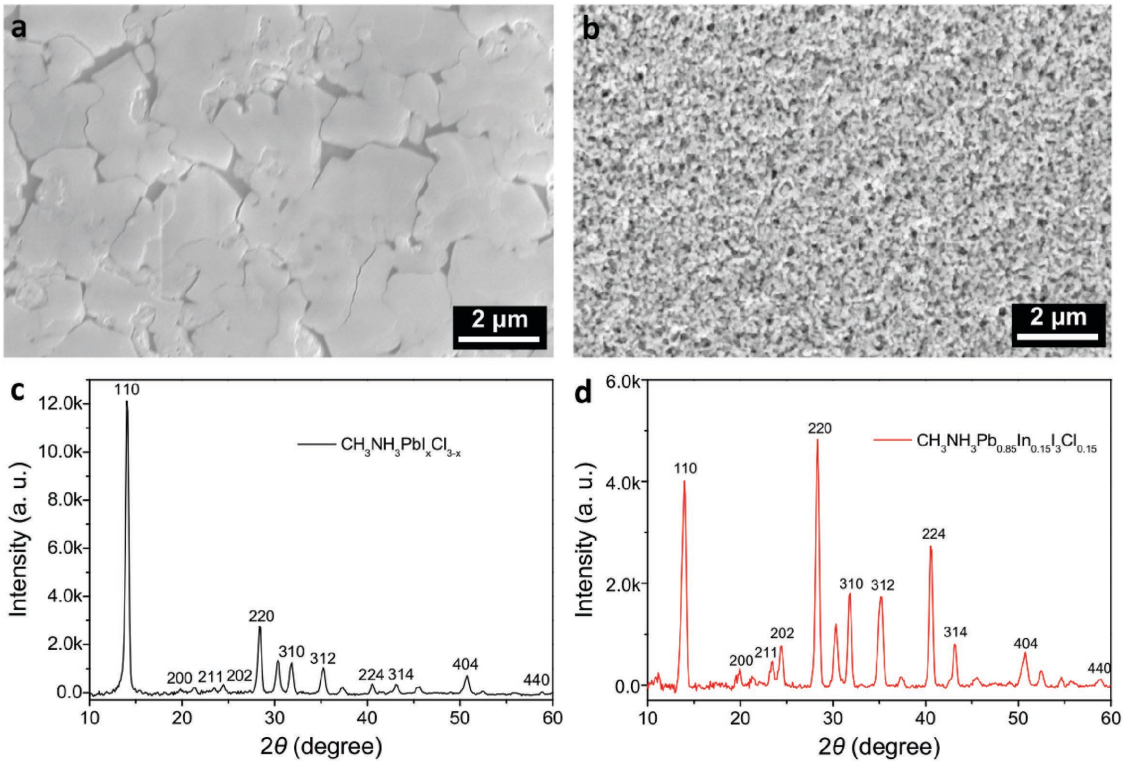

Figure 3. SEM images of (a) $CH_3NH_3PbI_xCl_{3-x}$ and (b) $CH_3NH_3Pb_{0.85}In_{0.15}I_3Cl_{0.15}$ perovskite films onto ITO/PEDOT:PSS underlayers. 1D XRD patterns of (c) $CH_3NH_3PbI_xCl_{3-x}$ and (d) $CH_3NH_3Pb_{0.85}In_{0.15}I_3Cl_{0.15}$ perovskite films onto ITO/PEDOT:PSS underlayers.

ratios, the presence of strongly scattered secondary spots and ring in Pb–In perovskites especially for $CH_3NH_3Pb_{0.85}In_{0.15}I_3Cl_{0.15}$ sample indicates that the crystalline domains were oriented relative to the plane of the substrate (Figure S8, Supporting Information). It suggests that suitable $InCl_3$ replacement could promote the perovskite growth with multiple ordered crystal orientations. With the increase of the $InCl_3$ ratio, the feature of multiple ordered crystallinity gradually vanished due to the appearance of PbI_2 (Figure S9, Supporting Information). The azimuthally integrated scattering intensity of different GIXRD patterns is plotted in Figure 4e along the ring at $q = 10$ nm^{-1} which is assigned to the (110) plane of corresponding perovskites structures, where q is the scattering vector ($q = 4\pi\sin(\theta)/\lambda$). Besides the sharp peaks at the azimuth angle of 90°, preferential orientations with obvious peaks at the azimuth angles of 4.5° (180° – 4.5°), 22° (180° – 22°), 26.5° (180° – 26.5°), 42.5° (180° – 42.5°), 52.5° (180° – 52.5°), 64.5° (180° – 64.5°), and 76.5° (180° – 76.5°) were observed in the Pb–In perovskites especially for $CH_3NH_3Pb_{0.85}In_{0.15}I_3Cl_{0.15}$ samples. These results indicate that there are three possible stacking ways for the grain crystal in the $CH_3NH_3Pb_{1-a}In_aI_3Cl_a$ films, which were illustrated visually in Figure 4f. Multiple ordered crystal orientations of Pb–In perovskites would result in efficient charge transport along multiple directions. Furthermore, hole- and electron-dominated devices were fabricated to evaluate the carrier mobility in pristine Pb and Pb–In perovskites by using space charge limited current method.[38–40] Compared to the hole mobility of 0.45 cm^2 V^{-1} s^{-1} and the electron mobility of 0.47 cm^2 V^{-1} s^{-1} in $CH_3NH_3PbI_xCl_{3-x}$, $CH_3NH_3Pb_{0.85}In_{0.15}I_3Cl_{0.15}$ perovskite films present improved charge transport characteristics with a hole mobility of 1.43 cm^2 V^{-1} s^{-1} and an electron mobility of 0.65 cm^2 V^{-1} s^{-1} (Figure S10, Supporting Information). We assumed it to be the main factor for substantially improved cell performance.

Introducing a suitable amount of $InCl_3$ into CH_3NH_3I- and $PbCl_2$-based perovskite precursor can make the perovskites grow along multiple directions, which results in the increase in the efficiency of Pb–In perovskite solar cells. The question still remains, though, what role $InCl_3$ plays in the Pb–In perovskites. Generally speaking, crystal growth is a complicated process. Recent studies have shown that the nucleation and growth of the perovskites mainly undergo two structural transitions including solution to precursor and precursor to perovskite.[41,42] Lead halide clusters formed in solution were reported to act as heterogeneous nucleation sites for the perovskite crystallization.[43,44] Currently, the detailed role of $InCl_3$ in the perovskite crystallization is difficult to be explained completely. Nevertheless, the presence or absence of In and Cl in final perovskite films can be identified easily by X-ray photoelectron spectroscopy (XPS) technique. **Figure 5**a,b shows the core levels of Cl $2p_{3/2}$ and In $3d_{5/2}$, respectively, in $CH_3NH_3PbI_xCl_{3-x}$ and $CH_3NH_3Pb_{0.85}In_{0.15}I_3Cl_{0.15}$. There is negligible amount of Cl element in the fully annealed $CH_3NH_3PbI_xCl_{3-x}$ film. One can speculate that Cl escaped from the film during the annealing process, agreeing well with the reported studies.[44–48] It should be noted that, despite undetectable Cl in annealed perovskites, the presence of Cl in precursor plays an important role in governing the crystallization process.[49–52] Notably, the core level of Cl $2p_{3/2}$ located at 199.2 eV, which is upshift by

Adv. Mater. 2016,
DOI: 10.1002/adma.201600626

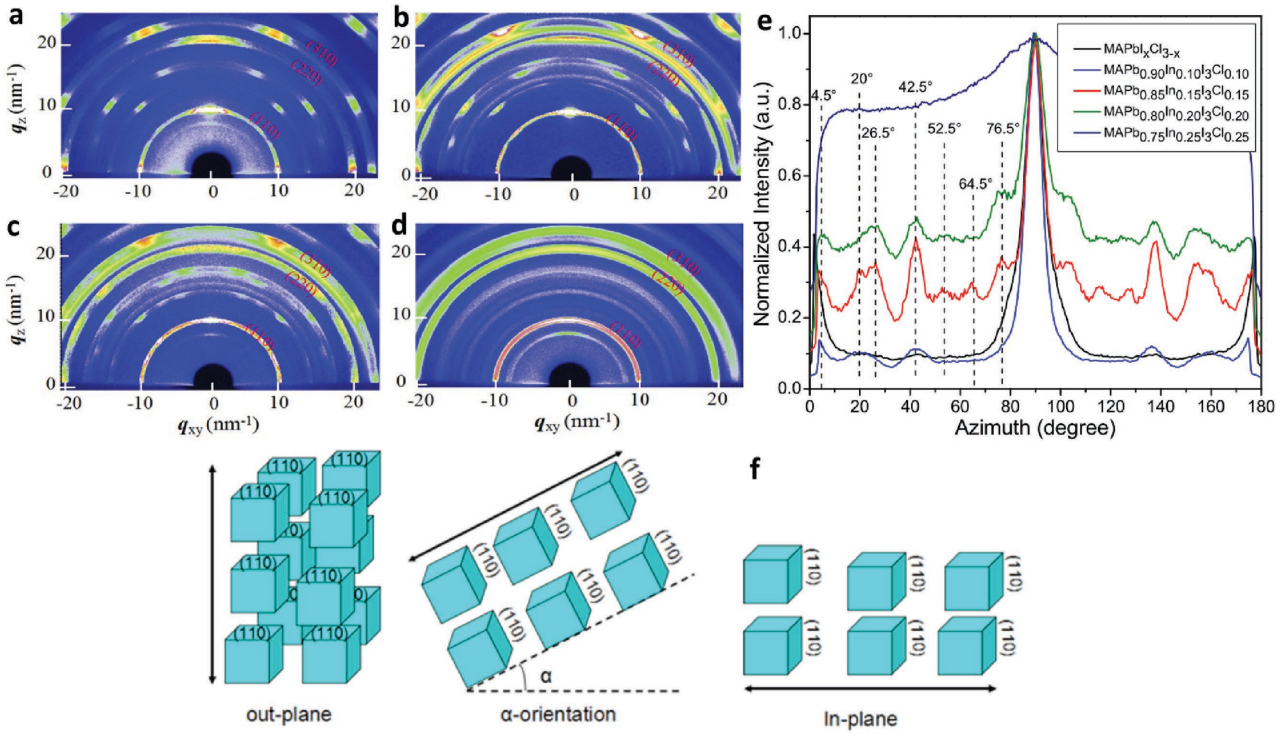

Figure 4. GIXRD patterns of (a) $CH_3NH_3PbI_xCl_{3-x}$, (b) $CH_3NH_3Pb_{0.90}In_{0.10}I_3Cl_{0.10}$, (c) $CH_3NH_3Pb_{0.85}In_{0.15}I_3Cl_{0.15}$, and (d) $CH_3NH_3Pb_{0.75}In_{0.25}I_3Cl_{0.25}$ perovskite films. e) Radially integrated intensity plots along the ring at $q = 10$ nm^{-1}, assigned to the (110) plane of $CH_3NH_3PbI_xCl_{3-x}$, $CH_3NH_3Pb_{0.90}In_{0.10}I_3Cl_{0.10}$, $CH_3NH_3Pb_{0.85}In_{0.15}I_3Cl_{0.15}$, $CH_3NH_3Pb_{0.80}In_{0.20}I_3Cl_{0.20}$, and $CH_3NH_3Pb_{0.75}In_{0.25}I_3Cl_{0.25}$ perovskite films. f) Three possible stacking ways for the grain crystal in the $CH_3NH_3Pb_{1-a}In_aI_3Cl_a$ films, where α is 4.5° (180° – 4.5°), 22° (180° – 22°), 26.5° (180° – 26.5°), 42.5° (180° – 42.5°), 52.5° (180° – 52.5°), 64.5° (180° – 64.5°), and 76.5° (180° – 76.5°).

0.3 eV related to 198.9 eV for that in pure $InCl_3$, is detected in $CH_3NH_3Pb_{0.85}In_{0.15}I_3Cl_{0.15}$. It means that Cl really exists in Pb–In perovskites after annealing. Similarly, as shown in Figure 5b, the core level of In $3d_{5/2}$ located at 446.3 eV, which is upshift by 0.3 eV related to 446.0 eV for that in pure $InCl_3$, is probed in $CH_3NH_3Pb_{0.85}In_{0.15}I_3Cl_{0.15}$. It reveals that In does present in annealed Pb–In perovskites. From XRD patterns (Figure S1, Supporting Information), no impurity byproducts of $InCl_3$ and/or InI_3 were observed even for those with large ratio of $PbCl_2$ replacement by $InCl_3$. The results of XRD and XPS suggest that the lead was substituted partially by indium in the Pb–In perovskites. Recent study reported that the presence of Cl could help minimize the morphological and energetic disorder of the perovskite films,[53] which is assumed to be one of the main factors for the small crystal size of the perovskites. We assume that this explanation was also feasible for the small crystal grains of Pb–In perovskites in the present case as shown in Figure 3b.

In a typical lead halide perovskite structure, the methylammonium (MA) cations locate in a random orientation within the octahedral $[PbX_6]^{4-}$ based inorganic cage.[54] The interactions (mainly of Coulomb and hydrogen bonds) between the NH_3 groups of the MA and the inorganic cage as well as the displacement of the organic cation strongly affect the crystallization process of perovskites.[53,55,56] In the present case, In and Cl in the Pb–In perovskites may cause a rearrangement of the locations of MA and inorganic cage, which would largely affect the orientation and displacement of the MA cations. Figure 5c shows the relative IR transmittance spectra of ≈300 nm thick $CH_3NH_3PbI_xCl_{3-x}$ and $CH_3NH_3Pb_{0.85}In_{0.15}I_3Cl_{0.15}$ films measured at normal incidence. The peaks (resonance frequencies of the vibrational modes) of 909 cm^{-1} (CH_3—NH_3^+, rock), 1467 cm^{-1} (symmetrical NH_3^+, bend), 1586 cm^{-1} (asymmetrical NH_3^+, bend), 3130 cm^{-1} (symmetrical NH_3^+, stretch), 3180 cm^{-1} (asymmetrical NH_3^+, stretch), which are in accordance with ref. [56] appear in both samples. Notably, the intensities of these MA-related rock, bend, and stretch modes in $CH_3NH_3Pb_{0.85}In_{0.15}I_xCl_{3-x}$ are obviously enhanced compared with the case of $CH_3NH_3PbI_xCl_{3-x}$ (Figure S11, Supporting Information). We attribute it to the influence of In and Cl which may cause more stronger interaction between the MA and the inorganic cage. Figure 5d shows the vibrational Raman spectra of two samples. In $CH_3NH_3PbI_xCl_{3-x}$, a broader peak at 94 cm^{-1} that represents the diagnostic modes of the inorganic cage[57] and a weak peak at 159 cm^{-1} assigned to the libration of MA cations[56] were observed. Interestingly, the inorganic cage based peak gets sharper and the MA cation based peak becomes stronger and more resolved with the $InCl_3$ ratio. Grancini et al. reported that a better resolved MA cation libration peak was associated with an ordered arrangement of the MA cations.[55–57] The preferential order of the organic cations in perovskites may slow down the rotational motion of the MA cations, inducing a multiple ordered crystal orientation (Figure 4e) of the perovskite crystalline grains. Despite the progress of several studies using IR and Raman,[53–59] the dynamic interplay between MA cation and the inorganic cage is still not fully understood currently. Currently, the issue is how do the In and Cl affect the

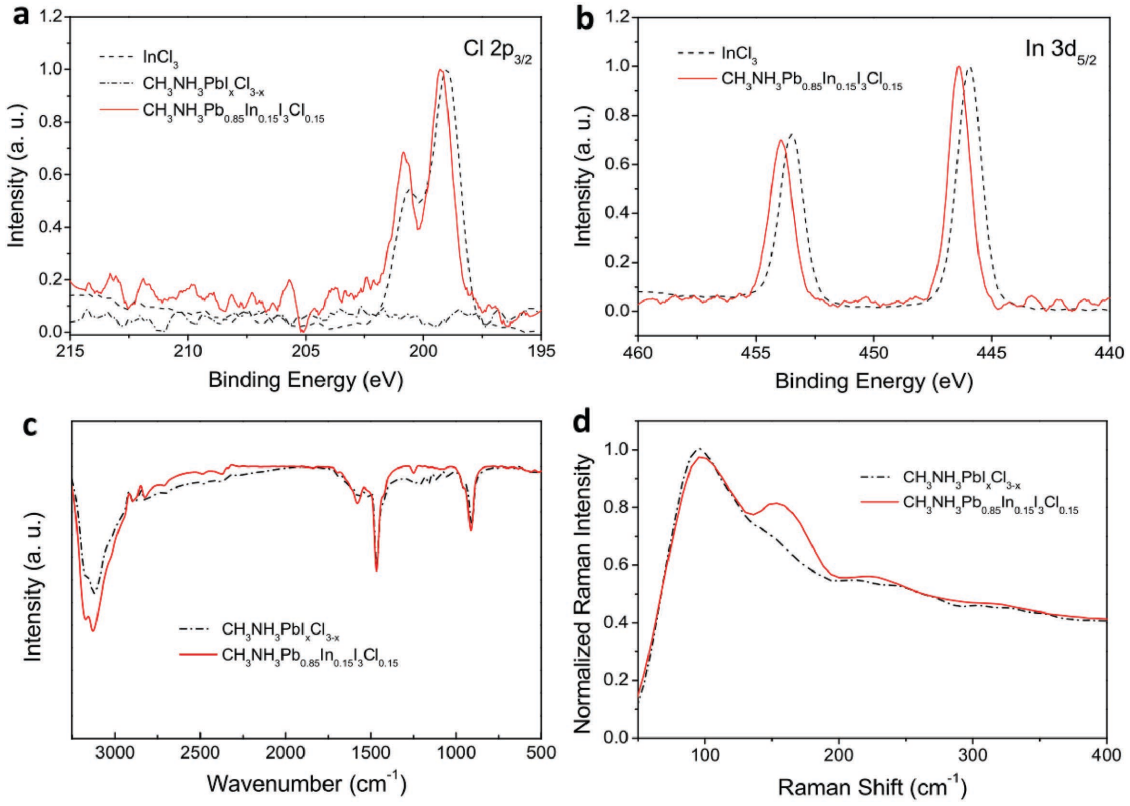

Figure 5. XPS data for (a) Cl $2p_{3/2}$ and (b) In $3d_{5/2}$ core level spectra in $InCl_3$, $CH_3NH_3PbI_xCl_{3-x}$, and $CH_3NH_3Pb_{0.85}In_{0.15}I_3Cl_{0.15}$ perovskites. c) Relative transmittance of $CH_3NH_3PbI_xCl_{3-x}$ and $CH_3NH_3Pb_{0.85}In_{0.15}I_3Cl_{0.15}$ films (deposited onto a Si wafer) measured at normal incidence using nonpolarized light. d) Resonant Raman spectra of $CH_3NH_3PbI_xCl_{3-x}$ and $CH_3NH_3Pb_{0.85}In_{0.15}I_3Cl_{0.15}$ films with a laser power intensity keeping in the order of 300 μW.

locations and the arrangement order of the MA cations and thus the perovskite crystallization is not understood completely. Further experiments and theoretical calculations are necessary to clarify the detailed mechanism in the future.

Finally, high-resolution GIXRD patterns of the Pb–In perovskites based on high brightness synchrotron radiation X-ray source were carried out to clarify the partial Pb^{2+} substitution by In^{3+}. **Figure 6**a presents the diffraction peaks of the (110) plane of $CH_3NH_3PbI_xCl_{3-x}$ and $CH_3NH_3Pb_{0.85}In_{0.15}I_3Cl_{0.15}$ perovskite films onto ITO/PEDOT:PSS underlayers. Compared with the $CH_3NH_3PbI_xCl_{3-x}$, the diffraction peak of the (110) plane of $CH_3NH_3Pb_{0.85}In_{0.15}I_3Cl_{0.15}$ shifts toward left from q = 10.0184 nm^{-1} to q = 10.0135 nm^{-1}. From the Bragg equation, the interplanar crystal spacing of (110) plane d_{110} is enlarged to 6.2747 Å ($CH_3NH_3Pb_{0.85}In_{0.15}I_3Cl_{0.15}$) from 6.1697 Å ($CH_3NH_3PbI_xCl_{3-x}$). It suggests that the partial replacement of $PbCl_2$ by $InCl_3$ caused the lattice expansion of the perovskites, which would be associated with the partial substitution of Pb^{2+} by In^{3+} or was caused by the microstress due to the $InCl_3$ introducing. Figure 6b shows the structural analysis of $CH_3NH_3Pb_{0.85}In_{0.15}I_3Cl_{0.15}$ perovskite films, mainly concentrated on (110) diffraction peak shown in Figure 6a. With a peak differentiation imitating for the (110) diffraction peak of $CH_3NH_3Pb_{0.85}In_{0.15}I_3Cl_{0.15}$ (by keeping one diffraction peak at q = 10.0184 nm^{-1} for $CH_3NH_3PbI_xCl_{3-x}$), a new diffraction peak at q = 9.9913 nm^{-1} is appeared, which corresponds to an interplanar crystal spacing of d_{110} = 6.2887 Å. The difference (0.119 Å) of the interplanar crystal spacing for the fitted two diffraction peaks corresponds to a change (0.1683 Å) of the lattice constant, which is very close to the difference (0.0907 Å) between the atomic radiuses of Pb (1.7497 Å) and In (1.6590 Å).[60] Considering the experimental error, the new diffraction peak at q = 9.9913 nm^{-1} is ascribed to the In-based perovskite due to the partial substitution of Pb by In. Therefore, we think that the lattice expansion of the Pb–In perovskites shown in Figure 6a was caused by the partial substitution of Pb^{2+} by In^{3+}.

In summary, we have demonstrated a success of binary Pb–In perovskite solar cells with simultaneously reduced Pb and improved cell performance. Pb–In perovskite films exhibit high quality with multiple ordered crystal orientations, which are beneficial for efficient charge transport along multiple directions and thus improved cell performance. The presence of In and Cl, which play an important role in governing the crystallization process and inducing the crystallization orientation, is confirmed in annealed Pb–In perovskites. The partial Pb^{2+} substitution by In^{3+} is clarified by high-resolution GIXRD based on high-brightness synchrotron radiation X-ray source. IR and Raman spectra demonstrate that Cl and In may cause stronger interaction between the MA cations and the inorganic cage, favoring a high order of MA cation arrangement with multiple ordered crystal orientations of perovskites. By optimizing the $InCl_3$ molar ratio, a promising PCE of 17.55% is achieved. Prior to the role of morphology control, the enhancement of the device performance is mostly associated

Adv. Mater. 2016,
DOI: 10.1002/adma.201600626

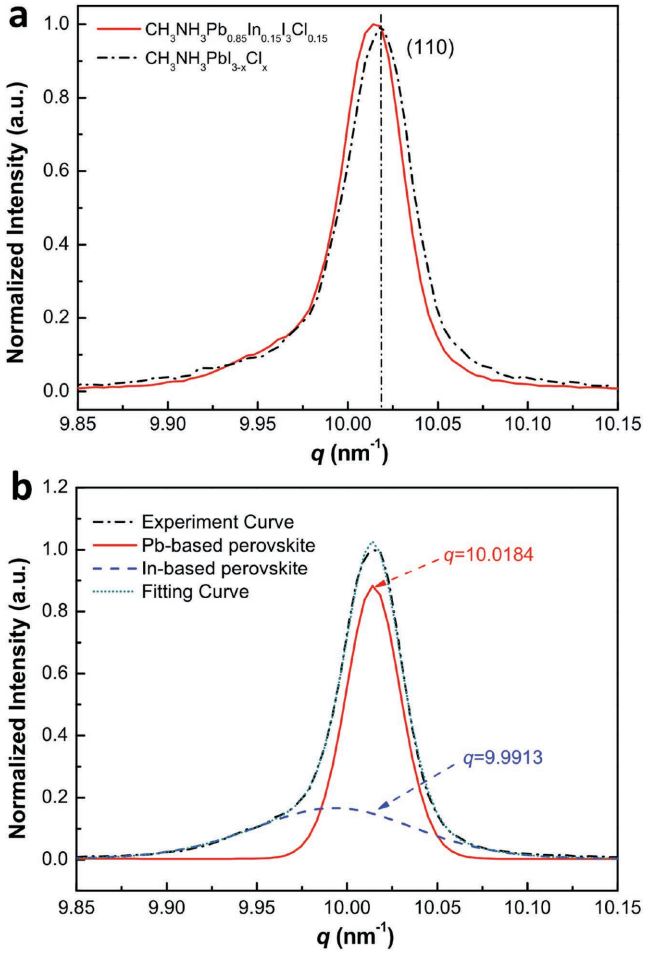

Figure 6. a) High-resolution X-ray diffraction peaks of the (110) plane of $CH_3NH_3PbI_xCl_{3-x}$ and $CH_3NH_3Pb_{0.85}In_{0.15}I_3Cl_{0.15}$ perovskite films onto ITO/PEDOT:PSS underlayers. b) Structural analysis of $CH_3NH_3Pb_{0.85}In_{0.15}I_3Cl_{0.15}$ perovskite films, mainly concentrated on (110) diffraction peak shown in panel (a).

with the feature of multiple ordered crystal orientation in the Pb–In perovskites. This work demonstrates the possibility of substituting the Pb(II) by using In(III) besides Sn(II), which opens a broad route to fabricate alloy perovskite solar cells with mitigated ecological impact.

Experimental Section

Materials: Methylammonium iodide (CH_3NH_3I) was prepared by reacting methylamine, 33 wt% in ethanol (Sigma-Aldrich), with hydroiodic acid (HI) 57 wt% in water (Sigma-Aldrich). HI was added dropwise at 0 °C for 2 h with magnetic stirring. Upon drying at 60 °C, a white powder was formed, which was dried overnight in a vacuum oven and purified with ethanol before use. To prepare perovskite precursor solution, MAI and lead chloride ($PbCl_2$, 98%, Aldrich) powder were mixed in anhydrous DMF (99.9%, Alfa-Aesar) with a molar ratio of 3:1. For the In-based perovskite precursor solution, MAI, $PbCl_2$, and indium chloride ($InCl_3$, 99%, Alfa-Aesar) powder were mixed with a desired molar ratio. The solutions (30 wt%) were stirred overnight in a glovebox at 60 °C. $PC_{61}BM$ and Bphen were purchased from Nichem Fine Technology Co., Ltd. (Taiwan).

Device Preparation: Devices were fabricated on patterned indium tin oxide (ITO) coated glass substrates with a sheet resistance of ≈15 Ω square^{-1}. ITO was cleaned with a neutral detergent, followed by a sonication in a bath containing ethanol and then treated in UV-ozone cleaner for 15 min. A PEDOT:PSS (Clevios P VP AI 4083, Heraeus) was spin-cast at 4500 rpm for 40 s on ITO substrates and dried at 140 °C for 10 min. For the perovskite layer, 30 wt.% $CH_3NH_3Pb_{1-a}In_aI_3Cl_a$ was spin-coated onto the hole transport layer at 4000 rpm for 40 s in an N_2 glovebox. The annealing of wet perovskite films was carried out by following a typical gradient increased temperature method that can be seen elsewhere. After it was dried at room temperature for ≈20 min, the samples were slowly heated from 60 to 100 °C at a ramp rate of 10 °C/10 min on a hot plate. After that, the electron-transporting layer ($PC_{61}BM$, 20 mg mL^{-1} in chlorobenzene) and Bphen interfacial layer (0.5 mg mL^{-1} in alcohol) were then sequentially deposited by spin-coating at 2000 rpm for 40 s and 4000 rpm for 40 s in an N_2 glovebox, respectively. Finally, the samples were transferred to a vacuum chamber for silver electrode evaporation. Silver (100 nm) was thermally deposited onto the Bphen layer under vacuum at 2×10^{-6} Torr through a shadow mask, defining a device area of 7.25 mm^2.

Characteristics: Conventional X-ray diffraction measurement was conducted using an analytical (Empyrean) apparatus. The GIXRD measurements were performed at the BL14B1 beamline of the Shanghai Synchrotron Radiation Facility using X-ray with a wavelength of 1.24 Å. 2D GIXRD patterns were acquired by a MarCCD mounted vertically at a distance ≈223 mm from the sample with a grazing incidence angle of 0.2° and an exposure time of 20 s. The 2D GIXRD patterns were analyzed using the FIT2D software and displayed in scattering vector q coordinates. A field-emission scanning electron microscope (Quanta 200 FEG, FEI Co.) was used to acquire SEM images. The absorbance of the perovskite films on PEDOT:PSS-coated ITO glasses was measured with a UV/vis spectrophotometer (PerkinElmer Lambda 750). The transmission IR spectrum was recorded from a Bruker Vertex 80v Fourier-transform infrared spectroscopy (FTIR) spectrometer in a nitrogen atmosphere or ambient air. Spectral resolution was set to 4 cm^{-1}, and all spectra were referenced to the spectrum of the bare Si substrate with natural oxide layer taken at the corresponding angle of incidence. Raman spectra were collected on an HR 800 Raman spectroscope (J Y, France) equipped with a synapse CCD detector and a confocal Olympus microscope. The spectrograph uses 600 g mm^{-1} gratings and a 532 nm He–Ne laser. The measurements were conducted at room temperature and in air. The laser power intensity was kept of the order of 300 μW in order to avoid sample degradation effects. XPS measurements were carried out in a Kratos AXIS Ultra-DLD ultrahigh vacuum surface analysis system. XPS measurements using a monochromatic Al K_α source (1486.6 eV) were conducted to study the charge-transfer conditions with a resolution of 0.4 eV. The *J–V* curves, including the reverse and forward scans (e.g., in Figure S11 of the Supporting Information), were measured (2400 Series SourceMeter, Keithley Instruments) under simulated Air-Mass (AM) 1.5 sunlight at 100 mW cm^{-2} (Newport, Class AAA solar simulator, 94023A-U). The incident photon-to-electron conversion efficiency (IPCE) measurement was performed using a system combining a xenon lamp, a monochromator, a chopper, and a lock-in amplifier together with a calibrated silicon photodetector.

Supporting Information

Supporting Information is available from the Wiley Online Library or from the author.

Acknowledgements

Z.K.W. and M.L. contributed equally to this work. The authors acknowledge financial support from the Natural Science Foundation of China (Grant Nos. 61307036, 61575136, and 11175239), the Natural

Science Foundation of Jiangsu Province (Grant No. BK20130288), the research grant (Grant No. 14DZ2261200) from the Science and Technology Commission of Shanghai Municipality, and the beamline BL14B1 at Shanghai Synchrotron Radiation Facility (SSRF) for providing the beam time. This project was also funded by the Collaborative Innovation Center of Suzhou Nano Science and Technology, and by the Priority Academic Program Development of Jiangsu Higher Education Institutions (PAPD).

Received: February 1, 2016
Revised: April 7, 2016
Published online:

[1] D. M. Chapin, C. S. Fuller, G. L. Pearson, *J. Appl. Phys.* **1954**, *25*, 676.
[2] M. A. Green, K. Emery, Y. Hishikawa, W. Warta, E. D. Dunlop, *Prog. Photovolt. Res. Appl.* **2015**, *23*, 1.
[3] S. D. Stranks, H. J. Snaith, *Nat. Nanotechnol.* **2015**, *10*, 391.
[4] H. Zhou, Y. Zhang, C. K. Mai, S. D. Collins, G. C. Bazan, T. Q. Nguyen, A. J. Heeger, *Adv. Mater.* **2015**, *27*, 1767.
[5] S. Mathew, A. Yella, P. Gao, R. Humphry-Baker, B. F. E. Curchod, N. Ashari-Astani, I. Tavernelli, U. Rothlisberger, M. K. Nazeeruddin, M. Grätzel, *Nat. Chem.* **2014**, *6*, 242.
[6] A. Kojima, K. Teshima, Y. Shirai, T. Miyasaka, *J. Am. Chem. Soc.* **2009**, *131*, 6050.
[7] S. Kazim, M. K. Nazeeruddin, M. Grätzel, S. Ahmad, *Angew. Chem. Int. Ed.* **2014**, *53*, 2812.
[8] H. J. Snaith, *J. Phys. Chem. Lett.* **2013**, *4*, 3623.
[9] N. G. Park, *J. Phys. Chem. Lett.* **2013**, *4*, 2423.
[10] P. Gao, M. Grätzel, M. K. Nazeeruddin, *Energy Environ. Sci.* **2014**, *7*, 2448.
[11] M. A. Green, T. Bein, *Nat. Mater.* **2015**, *14*, 559.
[12] National Renewable Energy Labs (NREL) efficiency chart; http://www.nrel.gov/ncpv/images/efficiency_chart.jpg (accessed: April 2015).
[13] W. S. Yang, J. H. Noh, N. J. Jeon, Y. C. Kim, S. Ryu, J. Seo, S. I. Seok, *Science* **2015**, *348*, 1234.
[14] N. Ahn, D. Y. Son, I. H. Jang, S. M. Kang, M. Choi, N. G. Park, *J. Am. Chem. Soc.* **2015**, *137*, 8696.
[15] Y. Ogomi, A. Morita, S. Tsukamoto, T. Saitho, N. Fujikawa, Q. Shen, T. Toyoda, K. Yoshino, S. S. Pandey, T. Ma, S. Hayase, *J. Phys. Chem. Lett.* **2014**, *5*, 1004.
[16] F. Hao, C. C. Stoumpos, D. H. Cao, R. P. Chang, M. G. Kanatzidis, *Nat. Photonics* **2014**, *8*, 489.
[17] F. Hao, C. C. Stoumpos, R. P. Chang, M. G. Kanatzidis, *J. Am. Chem. Soc.* **2014**, *136*, 8094.
[18] N. K. Noel, S. D. Stranks, A. Abate, C. Wehrenfennig, S. Guarnera, A. A. Haghighirad, A. Sadhanala, G. E. Eperon, S. K. Pathak, M. B. Johnston, A. Petrozza, L. M. Herz, H. J. Snaith, *Energy Environ. Sci.* **2014**, *7*, 3061.
[19] Q. Chen, H. Zhou, Z. Hong, S. Luo, H. Duan, H. Wang, Y. Liu, G. Li, Y. Yang, *J. Am. Chem. Soc.* **2013**, *136*, 622.
[20] F. Zuo, S. T. Williams, P. W. Liang, C. C. Chueh, C. Y. Liao, A. K. Y. Jen, *Adv. Mater.* **2014**, *26*, 6454.
[21] M. G. Ju, G. Sun, Y. Zhao, W. Liang, *Phys. Chem. Chem. Phys.* **2015**, *17*, 17679.
[22] H. J. Feng, T. R. Paudel, E. Y. Tsymbal, X. C. Zeng, *J. Am. Chem. Soc.* **2015**, *137*, 8227.
[23] U. Bansode, R. Naphade, O. Game, S. Agarkar, S. Ogale, *J. Phys. Chem. C* **2015**, *119*, 9177.
[24] X. Gong, M. Li, X. B. Shi, H. Ma, Z. K. Wang, L. S. Liao, *Adv. Funct. Mater.* **2015**, *25*, 6671.
[25] Y. H. Lou, M. Li, Z. K. Wang, *Appl. Phys. Lett.* **2016**, *108*, 053301.
[26] Z. K. Wang, M. Li, D. X. Yuan, X. B. Shi, H. Ma, L. S. Liao, *ACS Appl. Mater. Interfaces* **2015**, *7*, 9645.
[27] M. Qian, M. Li, X. Shi, H. Ma, Z. K. Wang, L. S. Liao, *J. Mater. Chem. A* **2015**, *3*, 13533.
[28] M. Saliba, K. W. Tan, H. Sai, D. T. Moore, T. Scott, W. Zhang, L. A. Estroff, U. Wiesner, H. J. Snaith, *J. Phys. Chem. C* **2014**, *188*, 17171.
[29] Z. Xiao, Q. Dong, C. Bi, Y. Shao, Y. Yuan, J. Huang, *Adv. Mater.* **2014**, *26*, 6503.
[30] D. T. Moore, K. W. Tan, H. Sai, K. P. Barteau, U. Wiesner, L. A. Estroff, *Chem. Mater.* **2015**, *27*, 3197.
[31] D. T. Moore, H. Sai, K. W. Tan, D.-M. Smilgies, W. Zhang, H. J. Snaith, U. Wiesner, L. A. Estroff, *J. Am. Chem. Soc.* **2015**, *137*, 2350.
[32] A. Dualeh, N. Tétreault, T. Moehl, P. Gao, M. K. Nazeeruddin, M. Grätzel, *Adv. Funct. Mater.* **2014**, *24*, 3250.
[33] S. T. Williams, C. C. Chueh, A. K. Y. Jen, *Small* **2015**, *11*, 3087.
[34] P. Zhao, J. Xu, X. Dong, L. Wang, W. Ren, L. Bian, A. Chang, *J. Phys. Chem. Lett.* **2015**, *6*, 2622.
[35] T. Y. Zhang, M. Yang, E. E. Benson, Z. Li, J. Lagemaat, J. M. Luther, Y. Yan, K. Zhu, Y. Zhao, *Chem. Commun.* **2013**, *51*, 7820.
[36] M. I. Saidaminov, A. L. Abdelhady, B. Murali, E. Alarousu, V. M. Burlakov, W. Peng, I. Dursun, L. Wang, Y. He, G. Maculan, A. Goriely, T. Wu, O. F. Mohammed, O. M. Bakr, *Nat. Commun.* **2015**, *6*, 1.
[37] Y. Dang, Y. Liu, Y. Sun, D. Yuan, X. Liu, W. Lu, G. Liu, H. Xia, X. Tao, *CrystEngComm* **2015**, *17*, 665.
[38] H. Wang, A. D. Sheikh, Q. Feng, F. Li, Y. Chen, W. Yu, E. Alarousu, C. Ma, M. A. Haque, D. Shi, Z. S. Wang, O. F. Mohammed, O. M. Bakr, T. Wu, *ACS Photonics* **2015**, *2*, 849.
[39] C. Wehrenfennig, G. E. Eperon, M. B. Johnston, H. J. Snaith, L. M. Herz, *Adv. Mater.* **2014**, *26*, 1584.
[40] Z. K. Wang, Y. H. Lou, S. Naka, H. Okada, *Appl. Phys. Lett.* **2011**, *98*, 063302.
[41] M. Saliba, K. W. Tan, H. Sai, D. T. Moore, T. Scott, W. Zhang, L. A. Estroff, U. Wiesner, H. J. Snaith, *J. Phys. Chem. C* **2014**, *118*, 17171.
[42] K. W. Tan, D. T. Moore, M. Saliba, H. Sai, L. A. Estroff, T. Hanrath, H. J. Snaith, U. Wiesner, *ACS Nano* **2014**, *8*, 4730.
[43] Y. Tidhar, E. Edri, H. Weissman, D. Zohar, G. Hodes, D. Cahen, B. Rybtchinski, S. Kirmayer, *J. Am. Chem. Soc.* **2014**, *136*, 13249.
[44] E. L. Unger, A. R. Bowring, C. J. Tassone, V. L. Pool, A. Gold-Parker, R. Cheacharoen, K. H. Stone, E. T. Hoke, M. F. Toney, M. D. McGehee, *Chem. Mater.* **2014**. *26*, 7158.
[45] Y. Zhao, K. Zhu, *J. Phys. Chem. C* **2014**, *118*, 9412.
[46] Y. Chen, Y. Zhao, Z. Liang, *Chem. Mater.* **2015**, *27*, 1448.
[47] A. Dualeh, N. Tétreault, T. Moehl, P. Gao, M. K. Nazeeruddin, M. Grätzel, *Adv. Funct. Mater.* **2014**, *24*, 3250.
[48] H. Yu, F. Wang, F. Xie, W. Li, J. Chen, N. Zhao, *Adv. Funct. Mater.* **2014**, *24*, 7102.
[49] S. Colella, E. Mosconi, P. Fedeli, A. Listorti, F. Gazza, F. Orlandi, P. Ferro, T. Besagni, A. Rizzo, G. Calestani, G. Gigli, F. D. Angelis, R. Mosca, *Chem. Mater.* **2013**, *25*, 4613.
[50] E. L. Unger, A. R. Bowring, C. J. Tassone, V. L. Pool, A. Gold-Parker, R. Cheacharoen, K. H. Stone, E. T. Hoke, M. F. Toney, M. D. McGehee, *Chem. Mater.* **2014**, *26*, 7158.
[51] S. Colella, E. Mosconi, G. Pellegrino, A. Alberti, V. L. P. Guerra, S. Masi, A. Listorti, A. Rizzo, G. G. Condorelli, F. D. Angelis, G. Gigli, *J. Phys. Chem. Lett.* **2014**, *5*, 3532.
[52] M. I. Dar, N. Arora, P. Gao, S. Ahmad, M. Grätzel, M. K. Nazeeruddin, *Nano Lett.* **2014**, *14*, 6991.
[53] G. Grancini, S. Marras, M. Prato, C. Giannini, C. Quarti, F. D. Angelis, M. D. Bastiani, G. E. Eperon, H. J. Snaith, L. Manna, A. Petrozza, *J. Phys. Chem. Lett.* **2014**, *5*, 3836.

[54] T. C. Sum, N. Mathews, *Energy Environ. Sci.* **2014**, *7*, 2518.
[55] E. Mosconi, C. Quarti, T. Ivanovska, G. Ruani, F. D. Angelis, *Phys. Chem. Chem. Phys.* **2014**, *16*, 16137.
[56] T. Glaser, C. Müller, M. Sendner, C. Krekeler, O. E. Semonin, T. D. Hull, O. Yaffe, J. S. Owen, W. Kowalsky, A. Pucci, R. Lovrinčić, *J. Phys. Chem. Lett.* **2015**, *6*, 2913.
[57] A. Stroppa, C. Quarti, F. D. Angelis, S. Picozzi, *J. Phys. Chem. Lett.* **2015**, *6*, 2223.
[58] B. W. Park, S. M. Jain, X. Zhang, A. Hagfeldt, G. Boschloo, T. Edvinsson, *ACS Nano* **2015**, *9*, 2088.
[59] M. Ledinský, P. Löper, B. Niesen, J. Holovský, S. J. Moon, J. H. Yum, S. D. Wolf, A. Fejfar, C. Ballif, *J. Phys. Chem. Lett.* **2015**, *6*, 401.
[60] O. N. Senko, D. B. Miracle, *Mater. Res. Bull.* **2001**, *36*, 2183.